JGR Solid Earth

RESEARCH ARTICLE

10.1029/2020JB020164

†Jiayuan Yao and Shaolin Liu contributed equally to this work.

Key Points:

- A joint inversion of regional and teleseismic P-wave traveltimes is performed in Myanmar
- A continuous Indian slab is imaged beneath central Myanmar, and the southern slab dips ~15° steeper than the northern one at >100 km depth
- We propose four possible models of the Indian Plate subduction system beneath central Myanmar

Supporting Information:

- Supporting Information S1

Correspondence to:

P. Tong,
tongping@ntu.edu.sg

Citation:

Yao, J., Liu, S., Wei, S., Hubbard, J., Huang, B.-S., Chen, M., & Tong, P. (2021). Slab models beneath Central Myanmar revealed by a Joint Inversion of regional and teleseismic traveltime data. *Journal of Geophysical Research: Solid Earth*, *126*, e2020JB020164. https://doi.org/10.1029/2020JB020164

Received 11 MAY 2020
Accepted 4 JAN 2021

Slab Models Beneath Central Myanmar Revealed by a Joint Inversion of Regional and Teleseismic Traveltime Data

Jiayuan Yao[1†], **Shaolin Liu**[1,2,3†], **Shengji Wei**[2,4], **Judith Hubbard**[2,4], **Bor-Shouh Huang**[5], **Meng Chen**[2], **and Ping Tong**[1,2,4]

[1]School of Physical and Mathematical Sciences, Division of Mathematical Sciences, Nanyang Technological University, Singapore, Singapore, [2]Earth Observatory of Singapore, Nanyang Technological University, Singapore, Singapore, [3]Institute of Crustal Dynamics, China Earthquake Administration, Beijing, China, [4]Asian School of the Environment, Nanyang Technological University, Singapore, Singapore, [5]Institute of Earth Sciences, Academia Sinica, Taipei, Taiwan

Abstract The intermediate-depth (50–180 km) seismicity beneath Myanmar provides direct evidence of the subducting Indian slab. However, the historic lack of regional seismic observations leads to previous low-resolution models that show large variations in slab geometry beneath Myanmar. The depth extent and morphology of the slab are still poorly known. In this study, we conduct a joint inversion of regional and teleseismic P-wave traveltimes from recently installed networks to image seismic velocity structures beneath central Myanmar by adopting an eikonal equation-based traveltime tomography method. The observations contain a total of 6,069 regional first *P*-wave arrivals and 29,787 teleseismic P-wave differential traveltimes. We find a high P-wave velocity anomaly beneath central Myanmar, which starts from ~50 km depth and extends continuously to the mantle transition zone (MTZ) and is interpreted as the subducting Indian slab. Below 100 km depth, the dip angle of the slab in the south is ~15° larger than that of the slab in the north, suggesting a possible slab tearing. Based on our tomographic results and previous studies, the slab in the north is inferred to have a deep stagnant segment lying above the 660-km discontinuity in the MTZ, but whether it is connected with the shallow dipping slab cannot be confirmed. Meanwhile, the slab in the south may just stay in the upper mantle (above 410 km), but it may also have penetrated the 410-km discontinuity. Taking into account all the scenarios, we propose four possible models of the Indian Plate subduction system beneath central Myanmar.

1. Introduction

Myanmar (Burma) occupies a complex tectonic region that plays a vital role in the geodynamic evolution of East Asia (Figure 1a). The elongated Burma Plate, which was first defined by Curray et al. (1979), connects the ongoing India-Asia continental collision along the Himalayan Range in the north to the subduction of the Indo-Australian Plate beneath the Sunda Plate in the south. The Rakhine-Bangladesh megathrust, that is, the northern extension of the Sunda megathrust, defines the western boundary of the Burma Plate, where it overrides the east-dipping Indian Plate. The Burma Plate is bounded to the east by the dextral strike-slip Sagging fault, which links to the Eastern Himalayan Syntaxis in the north and the spreading center of the Andaman Sea in the south. East of the Sagging fault lies the Shan plateau, which is accommodating distributed deformation along both sinistral and dextral strike-slip faults (Wang et al., 2014). The Burma Plate contains two noticeable north-south trending structures (Figures 1a–1b): (1) the Indo-Burman Range (IBR), which connects the Eastern Himalayan Syntaxis in the north with the Andaman-Nicobar Ridge and the outer arc ridge off Sumatra in the south; and (2) the Central Myanmar Basin (CMB), which extends southward into the central basin of the Andaman Sea. The subduction-related Indo-Burman Wedge (IBW) is bounded by the Rakhine-Bangladesh megathrust to the west and the CMB to the east (Figure 1a). The outer IBW is composed of Neogene clastic sequences affected by a series of asymmetric folds, and the inner IBW rises as the IBR (Mallick et al., 2019).

The existence of an eastward dipping subduction zone beneath Myanmar has been confirmed by seismicity (e.g., Hurukawa et al., 2012; Le Dain et al., 1984; Ni et al., 1989; Satyabala, 2003), seismic velocity anomaly (e.g., Fukao & Obayashi, 2013; Li et al., 2008; Pesicek et al., 2010; Replumaz et al., 2010; Tao et al., 2018), and gravity anomaly (Mitra et al., 2018). The eastward dipping Wadati-Benioff zone is well evidenced by the

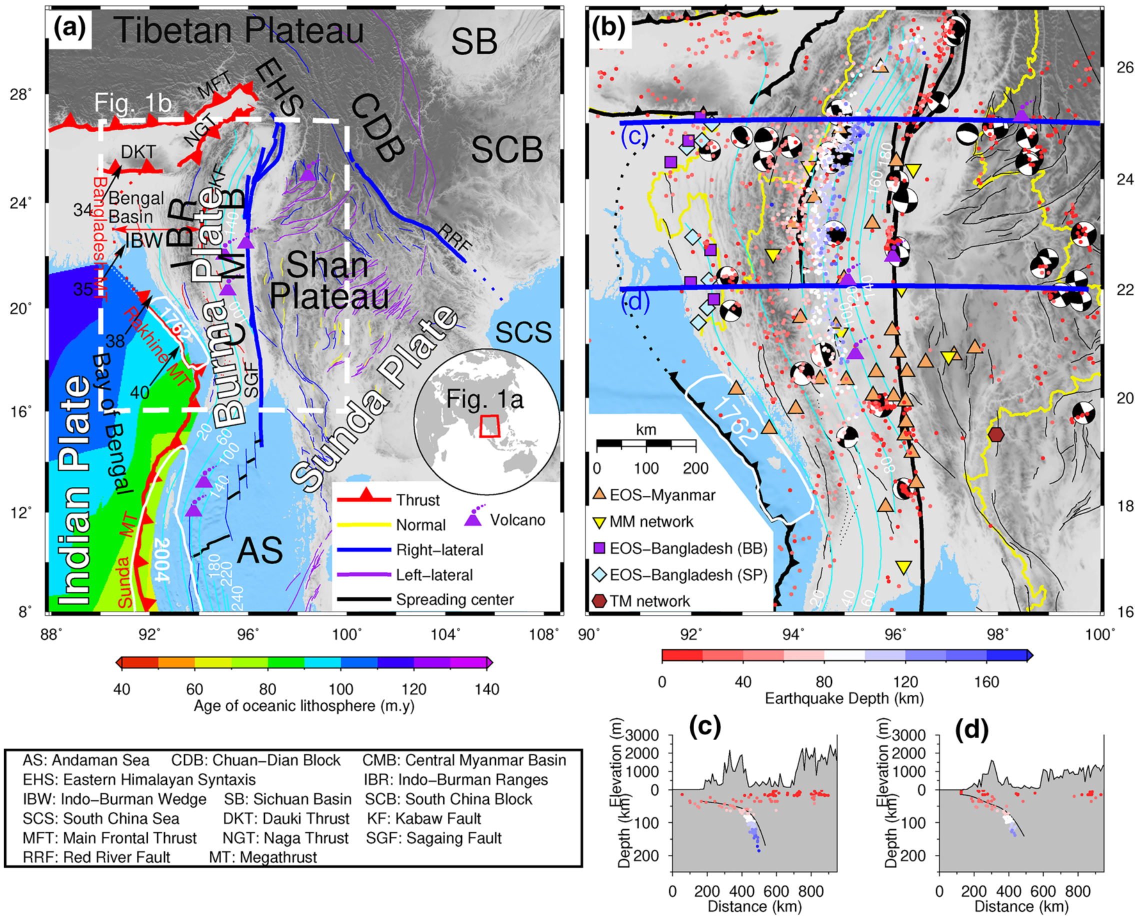

Figure 1. Tectonic setting in and around the study area. (a) Overview map in and around Myanmar. Major faults are modified from (Wang et al., 2014), and volcano locations are from Global Volcanism Program 2013 (https://doi.org/10.5479/si.GVP.VOTW4-2013) and VolcanoDiscovery (https://www.volcanodiscovery.com). The black arrows show the direction and magnitude (mm/year) of the relative motion of the Indian Plate with respect to the Shan plateau (Mallick et al., 2019). Slab contours (cyan lines) are modified from the Slab 2 model (Hayes, 2018). The rupture areas of the 1762 and 2004 megathrust earthquakes follow after Mallick et al. (2019) and Ishii et al. (2005), respectively. The age of the oceanic lithosphere is modified from Müller et al. (2008). The white dashed box indicates our study area, and the inset shows the location of Figure 1a. (b) Seismicity in the study region, with those along two vertical profiles (blue lines) shown in Figures 1c–1d. Earthquakes indicated by dots and color-coded with event depths are from the ISC-EHB catalog (1960–2016) (Engdahl et al., 1998) and the relocated regional earthquake catalog in this study (2016–2019). Double-couple solutions for earthquakes with *Mw* larger than 6.0 are downloaded from the GCMT catalog (1976–2018) (Ekström et al., 2012). Volcanos from the south to north are Popa, Monywa, Singu, and Tenchong, respectively. Seismic stations are color-coded with their network names. BB, Broadband, EOS, Earth Observatory of Singapore, MM, Myanmar National Seismic Network, SP, Short period, TM, Thai Seismic Monitoring Network. (c–d) Seismicity within a 30-km width of two vertical profiles shown in Figure 1b, along with slab geometries (black lines) within a 10-km width of each profile.

intermediate-depth seismicity beneath central and northern Myanmar, with a maximum earthquake depth of ~180 km (Figures 1b–1d). A high P-wave velocity anomaly beneath Myanmar, which is interpreted as the subducting Indian Plate, has also been imaged by both global- and continental-scale tomographic models. However, there are large variations in slab morphology and depth extent among these tomographic models. Depth profiles of two representative models, one from global P-wave traveltime tomography (Fukao & Obayashi, 2013) and one from regional waveform tomography (Tao et al., 2018), show high-velocity anomalies beneath Myanmar, but the slab geometry is generally poorly imaged, in particular beneath ~200 km depth, which happens to be near the depth extent of the seismicity (Figures S1 and S2, respectively). For instance, Fukao and Obayashi (2013) show a broad but weak high-velocity anomaly deeper than ~200 km along the 21–22° latitude profiles (Figure S1), which is barely connected to the better-imaged shallower part of the slab. The model of Tao et al. (2018) reveals a clear slab structure beneath most regions in Eastern Asia, but exhibits poorly-constrained results beneath Myanmar, with the shallow part (<200 km) of the slab barely imaged (Figure S2), probably because Myanmar is located at the edge of their model and thus is not well-resolved. In short, the lack of regional observations has led to previous low-resolution velocity models for the Myanmar region. Consequently, the subduction history of the Indian Plate beneath Myanmar is not well understood, although the large-scale four dimensional evolution of Southeast Asia's mantle has been inferred from geological reconstructions and seismic tomography (Replumaz et al., 2004).

Without a well-constrained subducting slab structure beneath Myanmar, our understanding of intra-slab seismicity and volcanism is also limited. Seismicity beneath Myanmar does not extend beyond a depth of ~180 km with decreasing earthquake termination depths from north to south (Figures 1b–1d), and thus a mechanism is needed to explain the fact that the base of seismicity is shallower than the depth extent of the subducting slab. The age of the Indian Plate oceanic lithosphere at the western coast of Myanmar is around 100 Ma (Figure 1a). Geodetic observations show active convergence between the Indian and Burma Plates across the IBW with an estimated east-west convergence rate of 13–17 mm/yr (Steckler et al., 2016) or 12–24 mm/yr (Mallick et al., 2019). With such an age and down-dip convergent rate, the Indian slab should be relatively cold beneath Myanmar, and therefore seismicity is expected throughout the slab in the upper mantle, which is not consistent with the observed seismicity depth extension. In addition, only three volcanoes can be found in Myanmar (Popa, Monywa, and Singu; Figures 1a and 1b; 2013), with the Holocene eruptions of calc-alkaline composition at Mt. Popa representing volcanological evidence of ongoing subduction of the Indian Plate (Belousov et al., 2018). One of the physical mechanisms of intermediate-depth earthquakes (>50 km) is dehydration embrittlement, probably indicating that the oceanic crust in the subducting Indian slab is actively dehydrating. However, it appears that beneath Myanmar, such inferred dehydration does not result in the large magma volumes that are commonly observed in other subduction zones.

High-resolution seismic imaging of the subducting slab and upper mantle structures would provide a basis for addressing these questions. Although a few seismic tomography studies have been conducted in this region, they are on the global or continental scale with a lateral resolution of more than 200 km (e.g., Fukao & Obayashi, 2013; Li et al., 2008), due to the lack of seismic data recorded in Myanmar. A few studies of the seismic structures of the upper crust have been conducted, mainly for petroleum exploration purposes, but those seismic profiles exist only in a few localized places with limited depth penetration (e.g., Pivnik et al., 1998). Thanks to recently installed seismic networks in the region, a refinement to the slab models beneath central Myanmar is now possible. In this study, we take advantage of these newly deployed seismic stations in Myanmar and Bangladesh along with some other regional stations to conduct an eikonal equation-based traveltime tomography study. We utilize P-wave traveltime observations from both regional and teleseismic events. A joint inversion of both data sets can provide more robust and comprehensive constraints on the seismic structures. We present the seismic data and inversion approach in Section 2, and the optimal tomographic model in Section 3, describe four possible models of the Indian Plate subduction system beneath central Myanmar and discuss the implications of our findings in Section 4.

2. Data and Methodology

We perform a joint inversion of regional and teleseismic P-wave arrival times in the study area, using an eikonal equation-based seismic tomography method with the following steps (S. Liu et al., 2019). First, we manually pick first P-wave arrival times of regional earthquakes and measure the differential traveltimes of teleseismic P-waves at every pair of nearby seismic stations via cross-correlation. We then relocate regional earthquakes using an initial three dimensional P-wave velocity model. This is followed by presenting the update to the initial three dimensional model obtained by inverting the P-wave arrival times of the relocated regional earthquakes. Finally, we perform teleseismic traveltime tomography to further improve the three dimensional velocity model.

2.1. Seismic Stations

We utilize P-wave traveltime observations recorded by seismic stations in Myanmar, Bangladesh, and Thailand (Figures 1b and Figures S3 and S4). The Earth Observatory of Singapore (EOS) has been maintaining a seismic monitoring network comprising 30 broadband seismic stations throughout Myanmar, most of which have been in operation since July 2017 (X. Wang et al., 2019). In addition, EOS has deployed six

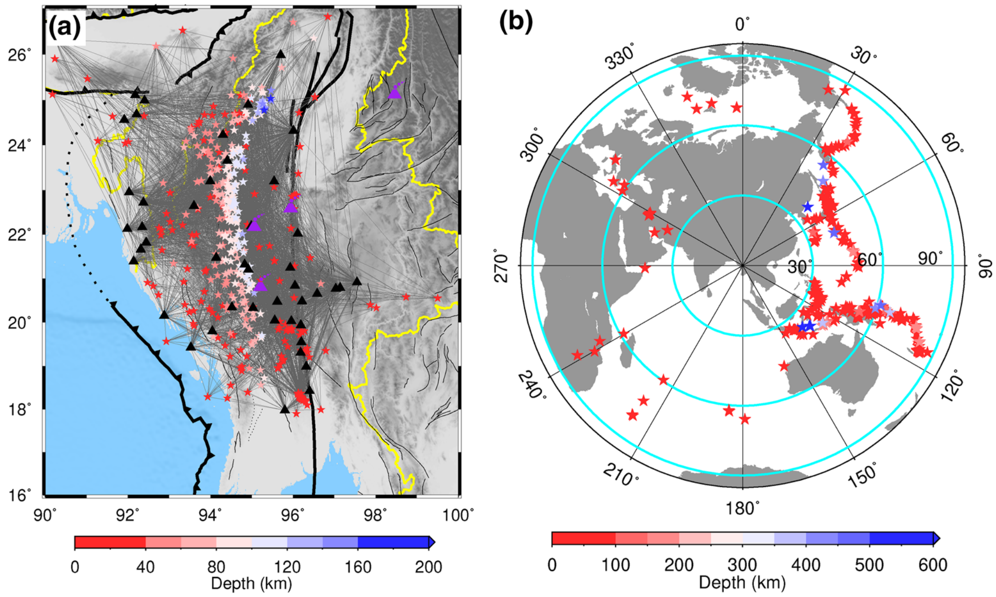

Figure 2. Map view of the regional and teleseismic events used in the seismic inversions. (a) P-wave raypaths (gray lines) from regional earthquakes (stars) to seismic stations (triangles). (b) Epicentral distribution of teleseismic events (stars).

broadband and 22 short-period seismic stations in eastern Bangladesh since June–September 2016. To increase the spatial coverage of the data, we also include some other seismic stations from the Myanmar National Seismic Network and Thai Seismic Monitoring Network. After evaluating data quality and addressing additional selection criteria to be discussed below, we finally choose seismic data from 50 seismic stations. These seismic stations provide high-quality P-wave traveltime observations with sufficient ray coverage for the joint regional and teleseismic traveltime tomography.

2.2. Seismic P-Wave Traveltime Measurements

We manually pick first P-wave arrivals of regional earthquakes which are automatically detected and located on continuous seismic waveforms by using the SeisComP3 software (Hanka et al., 2010). Seismic waveforms are processed with a bandpass filter between 1.5 and 5.0 Hz with two poles and one pass. Following this, the arrival time of every identifiable first P-wave is picked twice. If the difference between the two arrival times is greater than 0.2 s, the arrival time is picked for a third time; the P-wave is discarded if its third arrival time is not within 0.2 s of either of its first two picked arrival times. In both earthquake relocation and regional traveltime inversion, we use the arrival times picked at the second (if only picked twice) or third time (if picked three times). We therefore consider that there is a picking error of about 0.2 s. Moreover, each selected earthquake has to be recorded by at least seven stations, and each station has to record at least 40 earthquakes. In all, we obtain 6,069 first P-wave arrivals recorded by 45 stations from 463 regional earthquakes occurring between August 2016 and February 2019 (Figure 2a and Figure S4a).

We measure the differential traveltimes of teleseismic P-waves at every pair of nearby broadband seismic stations using the cross-correlation approach. Teleseismic events archived in the Advanced National Seismic System Comprehensive Earthquake Catalog (https://earthquake.usgs.gov/data/comcat) are used if their great-circle distances to the study area range from 25° to 95° and magnitudes exceed 5.5. The seismic waveforms are deconvolved with their instrument responses and bandpass filtered from 0.02 to 0.2 Hz with two poles and two passes (the discussion about the used frequency can be found in Text S1 in the supporting information). In our processing, we first automatically determine the arrival time of the maximum amplitude (peak or trough) in the interval that starts 5 s before and ends 10 s after the theoretical P-wave arrival time. Then, we calculate the differential traveltimes between all possible station pairs with station spacing less than 2.5°, applying the cross-correlation technique to the windowed waveforms. The time windows start at 10 s before and end at 20 s after the identified peaks or troughs. The differential traveltime is considered to be valid only if the corresponding cross-correlation coefficient is larger than 0.95 and the windowed waveforms both have a signal-noise-ratio larger than 2.0. The signal-noise-ratio is defined as the ratio of the average amplitudes between the signal and noise within a time window of 30 s, which start at 50 and 10 s before the identified peaks or troughs, respectively. These two criteria automatically keep only high-quality P-wave differential traveltime measurements. Each earthquake and seismic station must have at least 5 and 100 differential traveltime observations, respectively. In total, we collect 29,787 P-wave differential traveltime observations recorded at 43 stations from 315 earthquakes occurring between June 2016 and March 2019 (Figure 2b; Figures S4b and S6). The discussion about the ignorable influence of velocity anomalies outside of the study region on the measured differential traveltimes can be found in Text S2 in the Supporting information.

2.3. Seismic Tomographic Inversion Approach

The eikonal equation-based traveltime tomography method is utilized to jointly invert regional earthquake and teleseismic observations (S. Liu et al., 2019). The wavefront propagation inside the study region is simulated by numerically solving the eikonal equation with the fast marching method (Rawlinson et al., 2010; Rawlinson & Sambridge, 2005; Sethian & Popovici, 1999). The traveltime and raypath of the first arrival can be reliably calculated with such a numerical method even in complex heterogeneous media (Rawlinson et al., 2006). The conjugate gradient method is used to iteratively solve the damped least-square problem (Tong et al., 2014). A prescribed level of model perturbation is set so that the maximum perturbation at each iteration does not exceed that value and the model can be steadily updated in a relatively small step length (S. Liu et al., 2019; Tong et al., 2017). The optimal prescribed perturbation value is determined by the maximum curvature point of the L-curve, that is, the trade-off curve between the model variance and traveltime residual variance (Figures 3a–3e). We use the multiple-grid model parametrization which generally has a better or comparable performance in capturing the heterogeneous subsurface structures than a collocated grid (Tong et al., 2019). The multiple-grid model parametrization is formed by partially/fully shifting different grids from each other, while those grids can also have different grid spacings. In our tomographic inversion, five spatially shifted collocated grids are used to form the multiple-grid. During each iteration, the velocity model on each collocated grid is updated first, and then the average of all the updated models on those collocated grids is used as the input model of the next iteration. Checkerboard resolution tests are conducted first to estimate the resolution scale of our traveltime observations (Figure 4). The initial P-wave velocity model in the study region consists of two parts, that is, the top three dimensional crust and uppermost mantle model modified from Wang et al. (2019) (above 100 km) and the bottom mantle structure following the ak135 model (Kennett et al., 1995) (below 100 km) (Figure 5). Wang et al. (2019) developed the lithospheric three dimensional shear-velocity model based on a joint inversion of receiver functions, Rayleigh-wave H/V ratios and Rayleigh-wave dispersions, along with the velocities in the unsampled regions following the CRUST1.0 model (Laske et al., 2013; Figure 5). In their forward waveform modeling, they also obtained a P-wave velocity model by scaling the shear-wave velocity through an empirical relation (Equation 9 in Brocher, 2005). Considering that the locations of regional earthquakes are only roughly estimated using the ak135 model (Figures 3a–3b), the initial three dimensional P-wave velocity model is first used to relocate all the regional earthquakes (S. Liu et al., 2019). After that, we use a cascade scheme to perform the joint inversion: regional traveltime tomography is first conducted to build an accurate shallow velocity model, and then teleseismic traveltime tomography is performed to refine the deep part of the initial model (Figures S5 and S6; the discussion about different inversion strategies can be found in Text S3 in the supporting information). Text S4 in the supporting information presents discussion about little effect of station term corrections on the final inverted model based on the joint traveltime tomography. Regional earthquake locations and P-wave velocities are inverted simultaneously when we perform regional traveltime tomography. The regional earthquake locations are further constrained using the final optimal model after the teleseismic traveltime inversion (Figures S19–S21). The final P-wave velocity perturbations with respect to the initial three dimensional model (Figure 5) and with respect to the one dimensional reference ak135 model (Figures 5–7) are estimated.

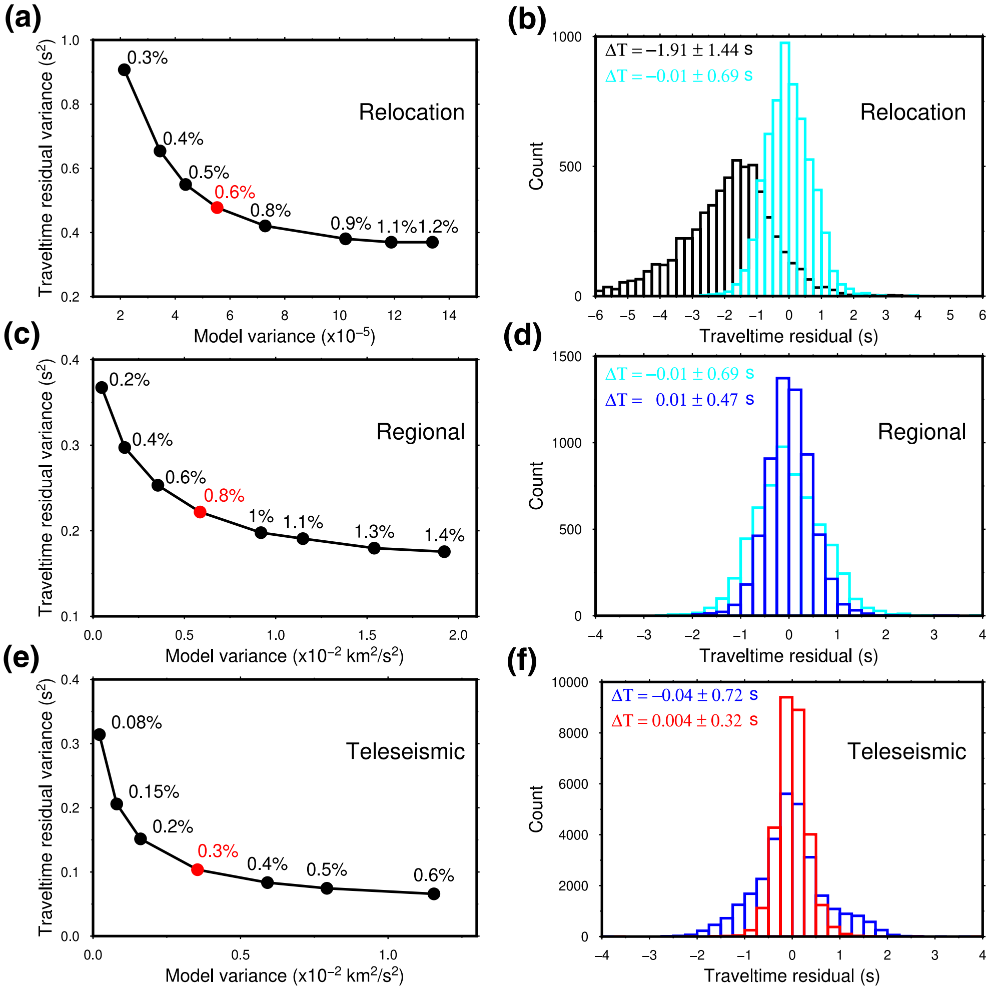

Figure 3. Trade-off *L*-curves between the model and traveltime residual variances (left panels) and frequency histograms of P-wave traveltime residuals (right panels). (a and b) *L*-curve and frequency histograms of regional earthquake traveltime residuals for regional earthquake relocation, (c and d) those for regional traveltime inversion, and (e and f) those of teleseismic differential traveltime residuals for teleseismic traveltime inversion. The red dots in the left panels denote the optimal maximum model perturbation values at each iteration. Dimensionless treatment is applied on the hypocentral coordinates and origin time, so the model variance in Figure 3a is dimensionless. The black (Figure 3b), cyan (Figure 3d) and blue (Figure 3f) histograms in the right panels are the traveltime residuals before the corresponding inversions, while the cyan (Figure 3b), blue (Figure 3d), and red (Figure 3f) histograms are those after the inversions. The averages and standard deviations of traveltime residuals are indicated in the top left and color-coded with the corresponding histograms.

3. Results

In this section, we present the optimal P-wave velocity model derived from the joint inversion. Checkerboard resolution tests are conducted first to find the optimal inversion grid and well-resolved regions in the model. Then, P-wave velocity anomalies are imaged through a joint inversion of regional and teleseismic data after an initial round of earthquake relocation. Text S5 in the supporting information contains additional resolution tests, which confirm the robustness of the optimal model by examining other factors that may influence the inversion, for example, the initial three dimensional velocity model for crustal traveltime corrections and the uneven earthquake distributions.

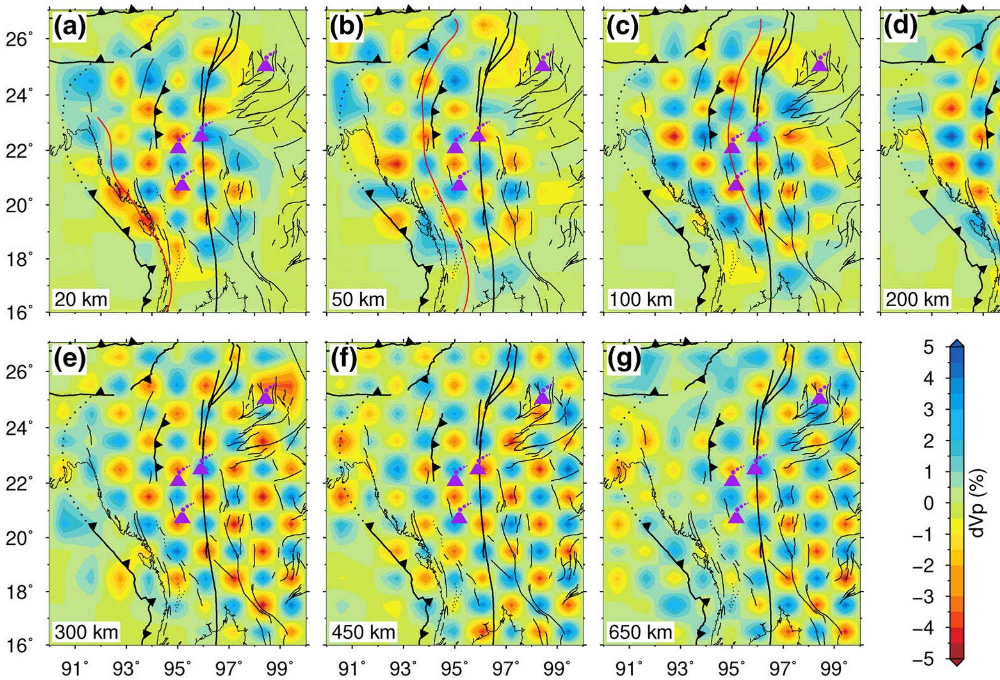

Figure 4. Checkerboard resolution test of the joint regional and teleseismic traveltime tomography (a–g). The recovered P-wave checkerboard model is obtained by inverting synthetic P-wave traveltimes that are added Gaussian noise with a standard deviation of 0.2 s. The input relative velocity perturbation is ±5%. The inversion procedure is the same as that for the real data (see the main text for the details).

3.1. Checkerboard Resolution Tests

Checkerboard resolution tests are conducted to estimate the resolving ability of our traveltime observations. A series of checkerboard tests with different inversion grid intervals allow us to find the optimal model parameterization. Alternate positive and negative relative velocity perturbations of 5% are assigned to the initial model. Then, the generated checkerboard model is used to calculate synthetic traveltimes, to which normally distributed random errors with a standard deviation of 0.2 s are added. The spatial distributions of the seismic stations and events used in the synthetic data are the same as those in the real data. The recovered checkerboard models are obtained by the joint inversion of regional and teleseismic synthetic data. The optimal lateral inversion grid intervals are 1.1° and 1.0° in the longitudinal and latitudinal directions, respectively (Figure 3). The inversion grid is set at 20, 50, 100, 200, 300, 450, and 650 km depths in the vertical direction. The synthetic model can be well-resolved at all depths beneath the CMB and in the upper mantle beneath the IBR, while the resolution beneath most regions in the Shan Plateau is poor above 200 km but relatively high below 200 km. The joint inversion of regional and teleseismic traveltime data can well constrain both shallow and deep structures, compared to individual inversions of each data set (Figure 4; Figures S7 and S9).

3.2. P-Wave Velocity Model and Interpretations

Regional earthquake relocation, regional and teleseismic traveltime tomography have greatly reduced both regional and teleseismic P-wave traveltime residuals at all the stations (Figure 3, Figures S20–S21 and S25–S27). The joint inversion performs better in resolving seismic structures as compared to individual inversions of each data set (Figure 6, Figures S8 and S10), as also shown in the checkerboard tests (Figure 4, Figures S7 and S9). The L-curve trade-offs are first estimated to determine the upper bounds of maximum model perturbations at each iteration for earthquake location, regional and teleseismic traveltime inversions (Figures 3a, 3c, and 3e and Figure S19a). The average and standard deviation of regional traveltime residuals decrease from −1.91 ± 1.44 s to −0.01 ± 0.69 s after regional earthquake relocation, and regional traveltime tomography further reduces them to 0.01 ± 0.47 s (Figures 3b and 3d). Traveltime residuals at almost all the stations decrease significantly after earthquake relocation and regional traveltime

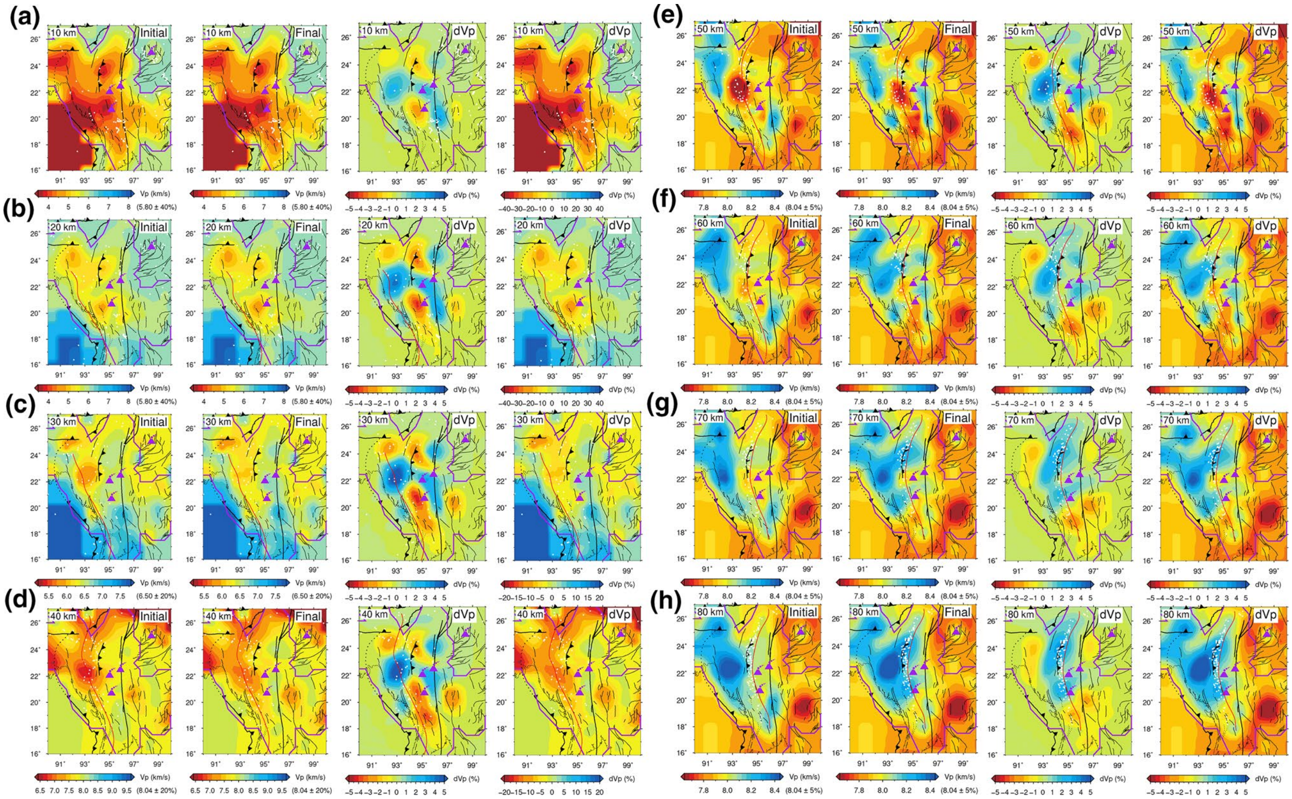

Figure 5. Map views of the P-wave velocity anomalies in the crust and uppermost mantle at eight depths (a–h). Absolute P-wave velocities in the initial and final three dimensional velocity models are displayed in the first and second columns, respectively. The central velocity (indicated near the color bar) in each color bar is near the P-wave velocity in the ak135 model (Kennett et al., 1995). P-wave velocity perturbations in the final model with respect to the initial three dimensional model and ak135 model are shown in the third and fourth columns, respectively. The velocities are the averages within a 5-km depth range of each slice. The white dots denote earthquakes occurred in the same depth range, while the purple volcano symbols indicate volcanos. Slab contours (red lines) are modified from the Slab2 model (Hayes, 2018). The inner and outer of the purple polygon indicate the initial three dimensional velocity model constrained by a joint inversion of multiple seismological data (X. Wang et al., 2019) and the part following the CRUST1.0 model, respectively (see the main text and Wang et al. (2019) for more details about the initial three dimensional model).

tomography (Figures S20a–S20c and S26). After teleseismic tomography, the average and standard deviation of teleseismic differential traveltime residuals decrease from −0.04 ± 0.72 s to 0.004 ± 0.32 s (Figure 3f), and traveltime residuals at each station have a noticeable decrease (Figures S25 and S27). The regional traveltime residuals barely change if a second round of earthquake relocation is performed in the final model (Figures S20d, S21b, and S26).

The final P-wave velocity model illuminates noticeable and interesting seismic structures in both shallow (crust and uppermost mantle [above 100 km]) and deep (below 100 km) parts of the study region (Figures 5–7). Since an initial three dimensional velocity model is used for the shallow part, we present velocity perturbations of the final model with respect to both the initial three dimensional model (the first three panels in Figures 5a–5h) and the ak135 model (the fourth panels in Figures 5a–5h, 6a, 6b, and 7). Velocity anomalies in the deep part are shown with respect to the ak135 model (Figures 6c–6g and 7).

The obtained shallow structures above 100 km shows complicated variations. Two high-velocity anomalies with maximum velocity perturbations of ~6% and 3.5% appear in the crust and uppermost mantle beneath the central IBR and beneath the volcano cluster of the CMB, respectively (the third panels in Figure 5). In addition, a low-velocity anomaly with a minimum negative velocity perturbation of −4.5% is located in the crust beneath the CMB west of Popa volcano (Figures 5a–5d). In the following text, the P-wave velocity perturbations are defined as those with respect to the global one dimensional ak135 model (the fourth panels in Figures 5a–5h, 6a, 6b, and 7). Low-velocity anomalies with a minimum negative velocity perturbation of −38% with respect to the ak135 model are noticeable beneath the CMB down to 10–20 km (Figures 5a,

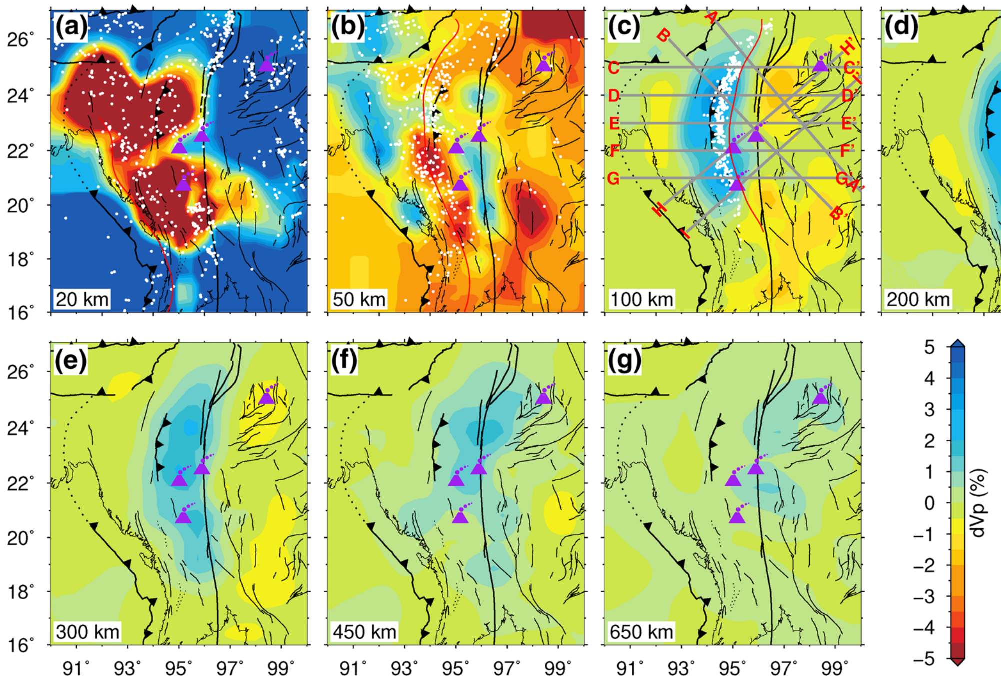

Figure 6. Map views of the final P-wave velocity model at seven depths (a–g). The velocity perturbations are plotted with respect to the ak135 model (Kennett et al., 1995). The white dots denote earthquakes that occurred at depths less than 20 km away from the slice, while the purple volcano symbols indicate volcanos. Vertical cross-sections of the P-wave velocity model along nine profiles (indicated by gray lines in Figure 6c) are shown in Figure 7. The red curves represent the slab contours modified from the Slab2 model (Hayes, 2018).

5b, and 6a). A low-velocity anomaly with a minimum negative velocity perturbation of −14% can be seen at a depth of ~40–50 km beneath the IBR west of the Myanmar volcano cluster (Figures 5d, 5e, and 6b). One high-velocity anomaly with a maximum velocity perturbation of ~20% appears beneath the central Sagging fault at a depth of about ~30–60 km (Figures 5c, 5f, and 6b). Another high-velocity anomaly with a maximum perturbation of 8% is observable beneath the central IBR at a depth of 50–80 km (Figures 5e–5h and 6b). Since an initial three dimensional velocity model is used and raypaths do not have a good coverage at shallow depths (i.e., crust and uppermost mantle), the inversion is still dominated by the initial three dimensional seismic features and less updated as compared with the deeper part. We emphasize here, however, that a good initial three dimensional velocity model for the crust is critical for reliable imaging of the deeper part.

The noticeable seismic feature in the deeper part of the model (below 100 km) is a crescent-shaped high-velocity anomaly with a maximum perturbation of ~4% beneath central Myanmar (Figures 6c–6g). This anomaly occupies the region from the IBR at 100 km depth to just the east of the Sagging fault at 450 km depth (Figures 6c–6f), while the northern segment even appears beneath Tengchong volcano at 650 km depth (Figures 6g and 7c). It seems that the deep high-velocity anomaly is connected to the shallow high-velocity anomaly beneath the central IBR (Figures 5e–5h, 6b and 7). The high-velocity seismic structures presented above are well-resolved with our regional and teleseismic traveltime data based on the checkerboard resolution tests (Figure 4). We interpret them as the subducting Indian slab. Compared with previous models (Figures S1 and S2), the present model shows a much clearer slab image, in particular at depths below ~100 km. At ~50–200 km, the high velocity anomalies agree well with the intra-slab seismicity, providing additional support to the robustness of our result. The dip angle of the slab changes dramatically from ~0° near the surface to ~55–70° at a depth of ~100 km (Figure 7). The possible continuity of the Indian slab down to a depth of ~450 km would require nearly 550 km of down-dip subduction in near E-W direction at a dip angle of 55°. If we assume that slab has gone down to ~450 km and a down-dip convergent rate of 12–24 mm/year has been more or less constant over time, subduction then has been ongoing since ~23–46 million years ago, roughly consistent with the beginning of India-Eurasian collision.

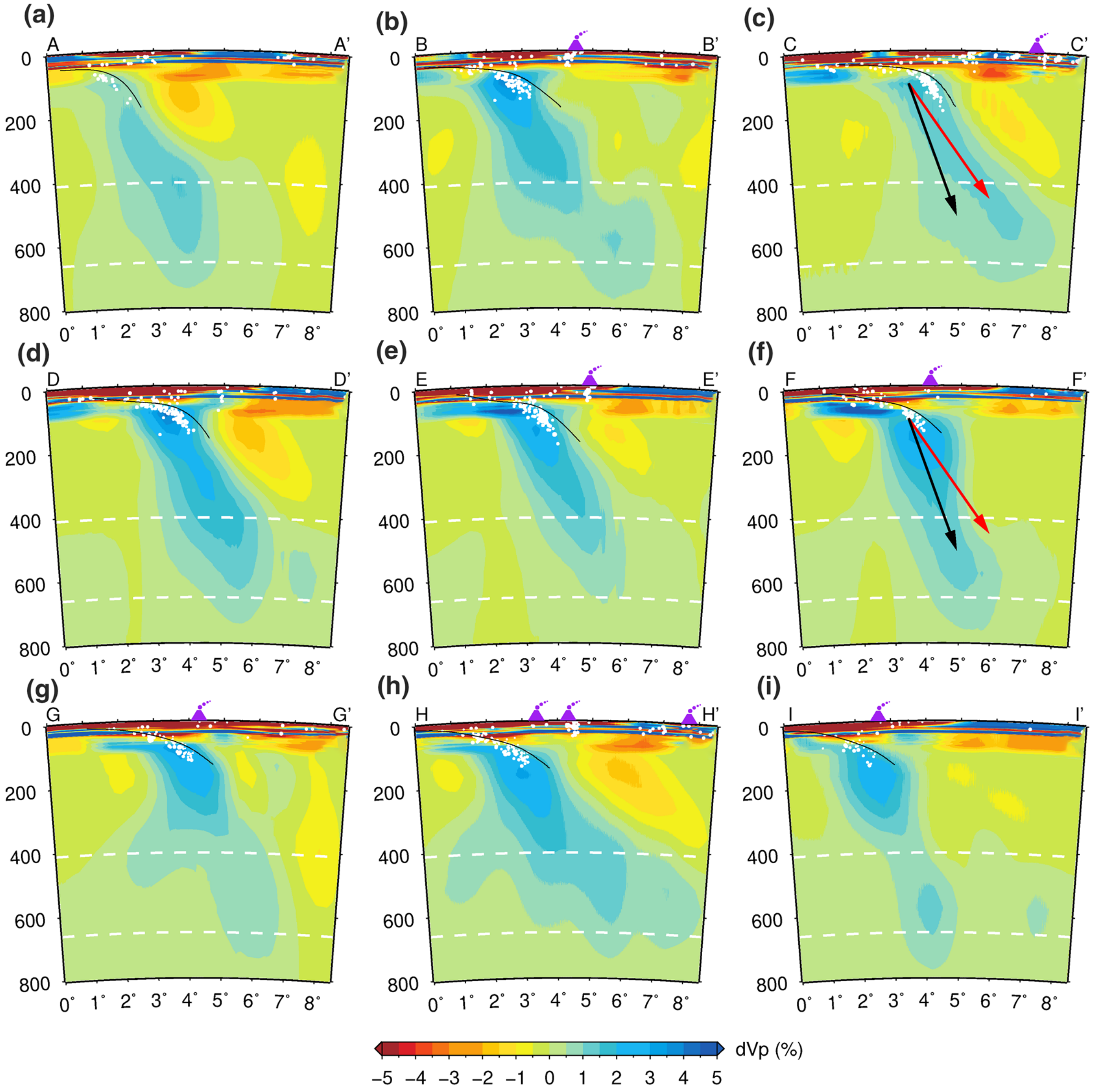

Figure 7. Vertical cross-sections in the final P-wave velocity model along nine profiles shown in Figure 6c (a–i). The white dots denote earthquakes occurring within a 30-km width of each profile, while the purple volcano symbols indicate volcanos within a 50-km width of each profile. Slab geometries (black lines) within a 10-km width of each profile are modified from the Slab2 model (Hayes, 2018), along with the 410- and 660-km discontinuities (white dashed lines). The red and black arrows indicate approximate dip angle of the high-velocity anomaly along the CC' and FF' profiles, respectively. Please note that the apparent wider high-velocity anomalies in the mantle transition zone in Figure 7h does not represent a wider slab, but it has a different orientation from the cross section in Figure 7g (please refer to Figures 6c and 6f for the locations of the vertical profiles).

One interesting feature of the slab image is its contrast with the seismicity depth. The seismicity terminates sharply at a depth of ~180 km beneath Myanmar (Figures 1b–1d), while the subducting slab might reach ~450 km and may even extend as deep as 600 km (Figures 6f, 6g, and 7). Disagreement between maximum intra-slab seismicity depth and depth extent of a subducting slab in the upper mantle is not uncommon (e.g., Hansen et al., 2019; Tao et al., 2018). In other subduction zones horizontal slab tearing is inferred to be one possible explanation (Hansen et al., 2019), but there is no noticeable slab tear in our tomographic model (Figures 6c–6d and 7c–7g). Thus, we speculate that the inconsistency between seismicity termination and slab penetration depths beneath Myanmar is caused by the failure of the physical mechanisms of deep earthquakes, for example, slab dehydration embrittlement or thermal shear runaway instability (Prieto et al., 2012). If hydrated minerals in the subducting slab complete phase changes to anhydrous forms at shallow depth, seismicity may not extend to deep depth (Hansen et al., 2019). The second possibility could be that the localization of shear strain cannot occur at deep depth. Therefore, the extent of the Wadati-Benioff zone does not reflect the termination of the subducting plate but rather where the slab cannot further dehydrate or does not support localization of shear strain (Hansen et al., 2019; Prieto et al., 2012). Besides, the observed decreasing earthquake termination depths from the northern to southern slabs (Figures 1b–1d) could indicate that there could be a gradual variation in physical properties (e.g., composition and/or temperature) of the subducting plate from north to south, which is consistent with the change of the lithosphere beneath the Bay of Bengal and the Bengal basin (Mitra et al., 2018; Singh et al., 2016; Figure 1a).

Another key feature in our model is the steep part of the high-velocity anomaly, which at depths greater than 100 km increases its dip southward from ∼55° for the northern segment to ∼70° for the southern segment (Figures 7c–7g). This change takes place at the latitude of ∼22°N, about 400 km north of the intersecting point between the Arakan (Rakhine) trench and the thick sediment in the Bay of Bengal. Due to the coverage of the sediment, the trench location was inferred from land based GPS observations (dashed line in Figure 1b; Mallick et al., 2019). Compared with the ophiolite belts located along the eastern edge of the IBR, this buried trench has been retreating further to the west than the southern segment, by up to 200 km. This faster trench retreat could be the key reason for the shallower dip angle of the subducting Indian slab north of 22°N, as shown in our tomography model. The subduction of the Indian Plate beneath Myanmar has a high degree of obliquity (∼60°), where GPS observations show that about 1 cm/year dextral shear was absorbed by the IBW (Mallick et al., 2019). Given this rate, the initiation of the dip angle difference could have started from a latitude that is south of its current position, for example, 0–3°, depending on when the faster trench retreat started. Besides, the dip change could also be related to a lateral shear stress within the subducting slab due to its oblique subduction east of the IBR (Mallick et al., 2019) and the variations of physical properties (e.g., composition and/or temperature) of the subducting slab. Oblique slab subduction can produce a trench-parallel shear stress within the slab, which would induce deformation of the subducting slab in the upper mantle and the MTZ (X. Liu et al., 1995). Thus, the oblique subduction (∼60°) may result in a large shear stress within the slab east of the IBR (Mallick et al., 2019), causing lateral dip angle change. The oblique subduction occurs below ∼100 km depth (Figure 6c), consistent with that of the abrupt slab dip change in the trench-normal direction (Figure 7). This type of slab deformation is also observed in northern Sumatra with a degree of oblique convergence of ∼70° (S. Liu et al., 2019). In addition, the variations of physical properties of the Indian slab may further contribute to its deformation which can cause the dip angle to increase from north to south. The southern subducting slab is oceanic with an age of ∼80–110 Ma (Figure 1a), but the origin of the northern one has not been seismologically constrained. For example, the crust beneath Bangladesh is reported to be oceanic (Singh et al., 2016) or transitional crust (Mitra et al., 2018), covered by thick sediment. Moreover, the difference in the slab dip angle indicates a possible slab tearing, which has been revealed in other subduction zones (e.g., S. Liu et al., 2019).

4. Discussion

Before further interpreting the features close to the edge of our model, we conduct a series of restoration resolution tests to further examine the resolution and robustness of the inversion. This procedure is similar to the checkerboard test, except that the targeting model is constructed based on the inverted seismic structures. Synthetic traveltimes are also added by normally distributed random errors with a standard deviation of 0.2 s. When the synthetic data are directly calculated in the final model, the recovered model is almost the same as our final model (Figure S28). Therefore, the regional and teleseismic traveltime datasets can at least resolve the parts of subsurface structure that resemble the final velocity model. However, this type of restoration test sometimes may not be able to distinguish real structures from possible artifacts. Therefore, we also generate several other synthetic models for restoration tests to check the reliability of the following features in the final model (Figure 8): (1) the depth extent of the deep high-velocity anomaly; (2) the geometry of the deep high-velocity anomaly; and (3) the dip angle of the deep high-velocity anomaly. Our results show that the northern deep high-velocity anomaly probably has penetrated into the mantle transition zone (MTZ), based on the fact that the recovered high-velocity anomaly (right panel in Figure 8a) reveals a very different pattern compared to the final model (Figure 7c) if the synthetic high-velocity anomaly is located above the MTZ (left panel in Figure 8a). However, these tests indicate that we cannot distinguish a model with a continuous high-velocity anomaly down to the 660-km from models with a flat segment lying above

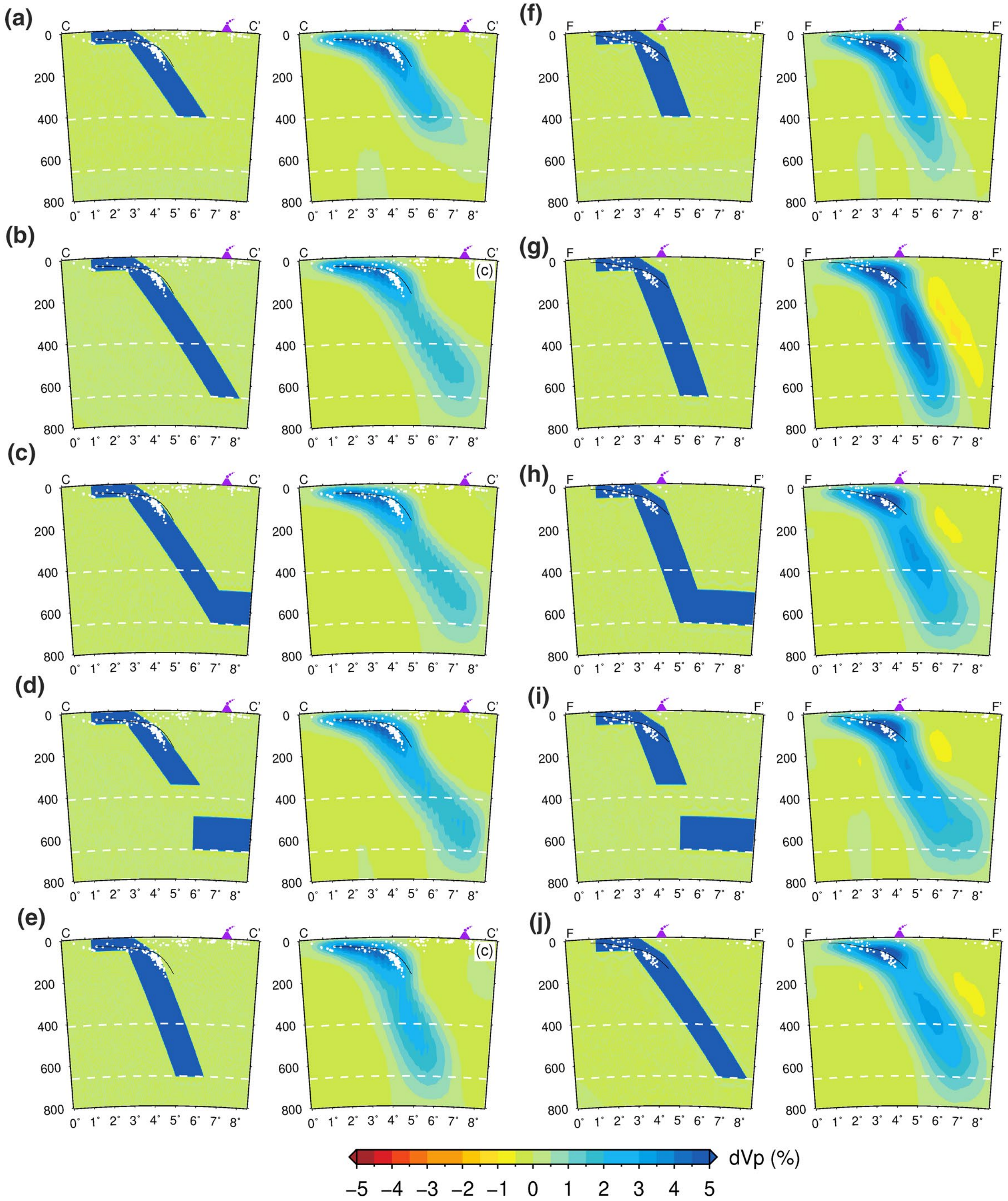

Figure 8. Restoration resolution tests for five different synthetic models at latitudes 25° (a–e) and 22° (f–j) (CC' and FF' profiles in Figure 7). Other symbols are the same as Figure 7.

the 660-km discontinuity in the MTZ (Figures 7c and 8b–8d). Moving to the south, restoration tests indicate that the recovered models for a flat high-velocity segment lying above the 660-km discontinuity in the MTZ (Figures 8h–8i) are different from the tomographic result for the southern segment (Figure 7f), but whether the anomaly penetrates into the MTZ cannot be resolved (Figures 7f and 8f–8g). Meanwhile, the dip angles for both northern and southern segments seem to be reliably resolved (Figures 7c, 7f, 8e, and 8j).

The imaged seismic P-wave velocity structures exhibit several interesting features, which can help us better understand the geodynamic evolution of the Myanmar region. The high-velocity anomaly at a depth of

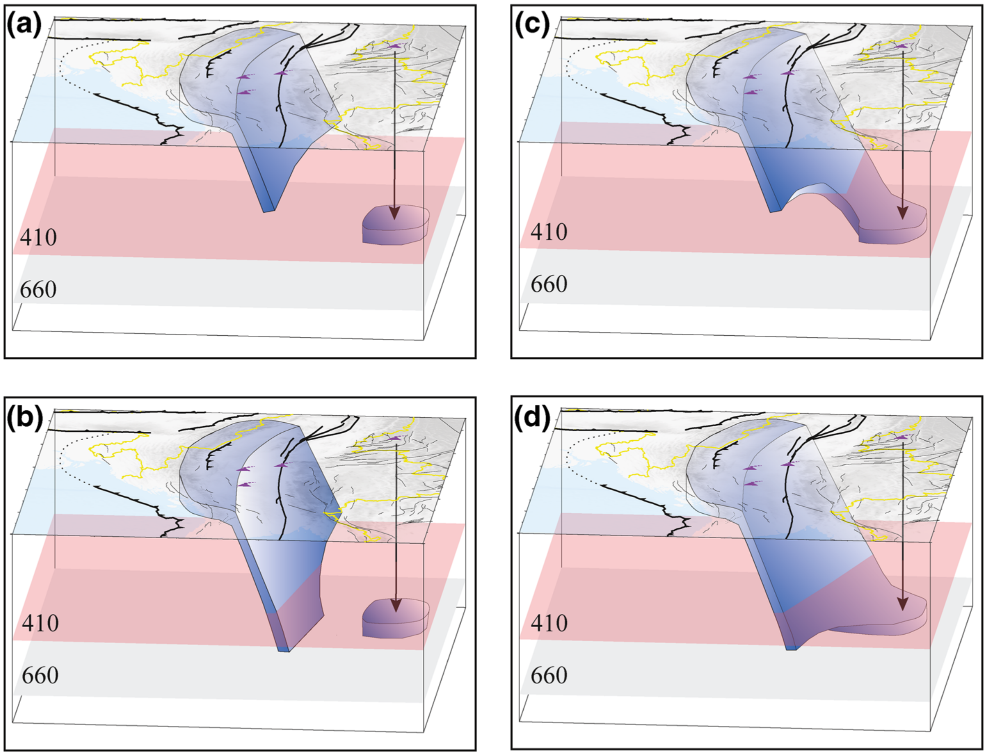

Figure 9. Illustrations of four possible models of the Indian Plate subduction system beneath central Myanmar (a–d). The 410- and 660-km discontinuities are indicated by the pink and gray planes, respectively. Other symbols are the same as Figure 1b. Note that the slab in the north could also possibly penetrate the 410-km discontinuity in Figures 9a and 9b.

~50 km beneath the central IBR is related to the deeper high-velocity anomaly below 100 km depth east of the IBR (Figures 5e–5h, 6b–6g, and 7). In the north, a high-velocity anomaly exists in the MTZ beneath Tengchong volcano, but whether it is connected to the high-velocity anomaly in the mantle above is not clear (Figures 7c and 8b–8d). In the south, a nearly vertical high-velocity anomaly is imaged in the deep part below 100 km, but whether it continues to the MTZ cannot be resolved either (Figures 7f and 8f–8g). Those high-velocity anomalies are related to the Indian Plate subduction beneath Myanmar (Fukao & Obayashi, 2013; Huang et al., 2019; Li et al., 2008; Pesicek et al., 2010; Replumaz et al., 2010; Tao et al., 2018; Figures S1–S2). The slab in the north may continuously subduct into the MTZ and may even become stagnant above the 660-km discontinuity in the MTZ (Figures 7c and 8b–8c). Previous studies reported high-velocity anomalies in the MTZ beneath Yunnan Province based on body-wave traveltime tomography with dense seismic data recorded in China (Huang et al., 2019; Lei & Zhao, 2016). Therefore, we regard that there is a flat stagnant slab in the MTZ beneath Tengchong volcano in our model, but a gap may exist between the shallow dipping slab and the deep flat slab, which is beyond the resolution of our inversion (Figures 7c and 8d). The slab in the south seems not to have a flat segment in the MTZ (Figures 7f and 8h–8i), but whether it has penetrated the 410-km discontinuity or not cannot be resolved by our data set (Figures 7f and 8f–8g).

Based on the inversion results and discussion above, we propose four possible models of the Indian Plate subduction system beneath central Myanmar, with multiple forms of segmentation in both horizontal and vertical directions during its oblique subduction. First, we consider two subducting slab models with a gap between the shallow dipping and the deep stagnant segments in the MTZ for the slab in the north (Figures 9a–9b). The shallow slab represents the recent Indian subducting plate, while the deep isolated slab may have a relationship to the shallow slab, but could also be a different tectonic slab, for example, a remnant Tethyan slab during the closure of the paleo-Tethyan ocean (Van der Voo et al., 1999). The difference between the two models is that the slab in the south may just stay in the upper mantle (Figure 9a) or have entered the MTZ (Figure 9b). In the latter case (Figure 9b), assuming that the isolated slab in the MTZ beneath Tengchong volcano was once connected to both the shallow slabs in the north and south, the gap among them could be caused by a near-horizontal slab tearing, possibly due to a difference in buoyancy. The inferred slab tearing is consistent with the lateral slab dip angle change from north to south as discussed in Section 3.2. The subducting slabs in the north and south could have different physical properties, with the former being transitional (Mitra et al., 2018) or oceanic (Singh et al., 2016) and the latter being oceanic (Figure 1a). If the deep isolated slab represents the old subducted oceanic Indian Plate similar to the subducting slab in the south, there could exist a difference in buoyancy between the shallow dipping and the deep stagnant slab segments due to composition difference, thus producing a near-horizontal slab tearing. The possible buoyancy difference due to composition difference between the slabs in the north and south may also explain their dip angle difference, that is, 15° (Figures 7c and 7f), with the slab in the south having larger negative buoyancy and thus a steeper dip angle. Second, we consider two subducting slab models with a continuous slab in the north (Figures 9c–9d). In this scenario, the subducting slab in the north becomes stagnant above the 660-km discontinuity in the MTZ. The slab in the south could either only exist in the upper mantle (Figure 9c), or it could also have penetrated the 410-km discontinuity (Figure 9d). The change of depth extent of the subducting Indian slab is then consistent with the decreasing trend of earthquake termination depth from north to south (Figures 1b–1d).

There are no clear low velocity structures beneath the volcanoes in central Myanmar at a depth of 50 km or deeper. A lack of low velocity zones in and above the asthenosphere indicates that large volumes of partially melted materials do not exist. This may, explain the very sparse volcanoes in Myanmar compared with other subduction zones. It is widely accepted that dehydration of the subducting slab and its interaction with the asthenosphere produces the magmas that feed volcanoes in subduction zones (Davies & Stevenson, 1992). However, the perpendicular to the trench convection cell involved in this mechanism would need further examination in the Myanmar region, due to the highly oblique subduction of the Indian Plate. Here the Burma Plate is moving along the Sagging fault at ~2 cm/year while the down-dip convergence in trench-perpendicular direction (near E-W) is only ~1 cm/year (Mallick et al., 2019). Therefore, the mantle flow beneath Myanmar is dominated by the near N-S direction motions, including that within the asthenosphere. The intermediate-depth earthquake could indicate that dehydration in the slab is still active down to a depth of at least 180 km, hence, the supply of water, either in free phase or hydrous phase, still exists there. The strong northward mantle flow slows down the circulation of higher temperature asthenosphere material within the slab system, therefore the temperature of the asthenosphere above the slab is probably lower than the amphibole-buffered peridotite solidus, which in turn prevents large volume partial melting. This mechanism could be verified by (or generalized to) the volcanism in other oblique subduction zones.

The origin of Tengchong volcano, an active volcano in southwest China which erupted in 1,609, is still under debate. It may have a deep origin associated with slab dehydration in the MTZ and induced mantle convection related to Indian Plate subduction (Huang et al., 2019; Lei & Zhao, 2016; Figure 10). This mechanism requests a continuous slab with a stagnant fragment lying above the 660-km discontinuity. Alternatively, melts could be produced by decompression, associated with a possible slab window between the subducting Indian slab in the upper mantle and the stagnant slab in the MTZ (Xu et al., 2018). In this scenario, the sinking slab could induce mantle upwelling in a return flow system, resulting in decompression melting in the upper mantle (Faccenna et al., 2010). This mechanism implies a gap between the shallow dipping slab and the deep stagnant one in the MTZ. The restoration tests indicate that our seismic observations cannot resolve these two mechanisms due to that seismic data recorded in China are not used by the present study (Figures 8c–8d), although it seems that the slab-related high P-wave velocity anomaly in our tomographic model is consistent with that reported by Huang et al. (2019) along the east-west profile beneath the volcano (Figure 10). A future study, needs to be conducted by simultaneously inverting seismic data in Myanmar and China to further resolve origin of the intraplate volcano.

It is interesting and important to extend the model resolution further to the south to cover the northern extension of the Sunda megathrust. Since the intermediate-depth seismicity in Myanmar ceases around the Yangon area (Pesicek et al., 2010), it is believed that the Rakhine-Bangladesh megathrust is bounded by a possible near-vertical tear in the subducting plate between Myanmar and the Andaman Sea (Richards et al., 2007). We note that no high P-wave velocity anomaly is observed there (Replumaz et al., 2010; Richards et al., 2007). Further south, the slab beneath the Andaman Sea has a steep dip angle as revealed by

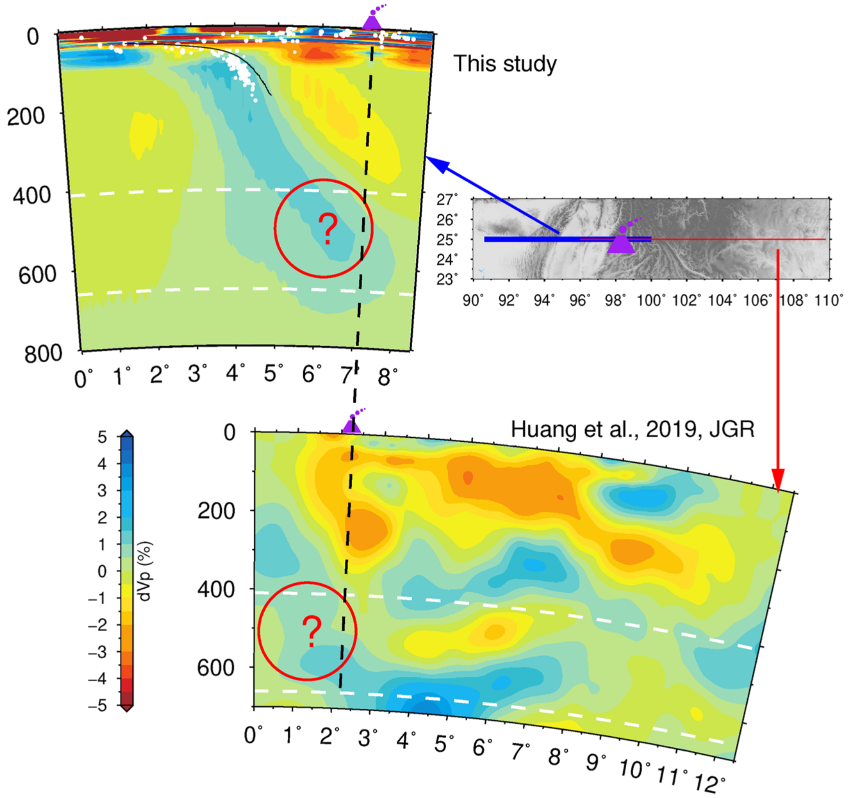

Figure 10. Comparison between P-wave velocity anomalies in this study (top left inset) and Huang et al. (2019) (bottom inset) along two vertical profiles (blue and red lines in the top right inset). Symbols are the same as Figure 7. The top velocity profile is the same as Figure 7c.

previous seismic tomographic studies (Pesicek et al., 2010; Replumaz et al., 2010) and the spatial distribution of seismicity (Singha et al., 2019), which is similar to that observed beneath central Myanmar in this study. Recently, Mishra et al. (2019) reported that the steeply subducting Indian slab beneath the Andaman Sea has penetrated through the 410-km discontinuity but terminates above the 660-km discontinuity based on their receiver function study. Our tomographic model indicates that the Indian slab may have penetrated the 410-km discontinuity beneath central Myanmar, but its termination depth cannot be resolved. A future survey is needed to explore the detailed slab geometry and the physical mechanism of the inferred slab tearing between beneath Myanmar and the Andaman Sea, by analyzing seismic data recorded in both Myanmar and the Andaman Sea.

5. Conclusions

We conduct an eikonal equation-based joint inversion of regional and teleseismic P-wave traveltimes to explore seismic structures beneath central Myanmar. The observations consist of a total of 6,069 handpicked first P-wave arrivals from 463 regional earthquakes and 29,787 P-wave differential traveltimes at every pair of nearby stations from 315 teleseismic events via the cross-correlation approach. A cascade scheme is used to perform the joint inversion: first, regional traveltime tomography is conducted to build an accurate shallow velocity model, and then teleseismic tomography is performed to refine the deep part of the initial velocity model. High P-wave velocity anomalies are inferred to appear from ~50 km depth to the MTZ, which is explained as the subducting Indian slab beneath Myanmar. The disagreement between maximum seismicity depth (~180 km) and depth extent of the imaged slab could indicate that the extent of the Wadati-Benioff zone does not reflect the termination of the subducting plate but rather where the slab cannot further dehydrate or does not support localization of shear strain. Below 100 km depth, the slab increases its dip southward from ~55° for the northern segment to ~70° for the southern segment, suggesting a possible slab tearing. Such a dip change can be explained by trench retreat and/or lateral shear stress within the subducting slab and variations of its physical properties. Based on the restoration tests and previous studies, the slab in the north could have a gap between the shallow dipping segment and the deep stagnant segment lying above the 660-km discontinuity in the MTZ, but could also be a continuous slab. Meanwhile, the slab in the south may just stay in the upper mantle, but may also have penetrated the 410-km discontinuity. Thus, we propose four possible models of the Indian Plate subduction system beneath central Myanmar to reflect the slab structures in this region.

Data Availability Statement

All of the figures are made using GMT (Wessel & Smith, 1998), while Figure 9 is further modified via Illustrator (https://www.adobe.com/products/illustrator.html). WebPlotDigitizer (https://automeris.io/WebPlotDigitizer) is used to digitalize the tectonic setting as in Figure 1. The observed arrival times of the regional and teleseismic events used here are available at the Nanyang Technological University research data repository (https://doi.org/10.21979/N9/EMYOEP). This work comprises Earth Observatory of Singapore contribution no. 288.

Acknowledgments
The authors thank Paul Tapponnier and Rishav Mallick for useful discussions. This research is partly supported by the National Research Foundation Singapore and the Singapore Ministry of Education under the Research Centers of Excellence Initiative (Project Code Number: 04MNS001913A620, M4430239.B50). This work is also partly funded by MOE AcRF Tier-1 Grant (04MNP000213C230) and MOE AcRF Tier-2 Grant (04MNP000797C230).

References

Belousov, A., Belousova, M., Zaw, K., Streck, M. J., Bindeman, I., Meffre, S., & Vasconcelos, P. (2018). Holocene eruptions of Mt. Popa, Myanmar: Volcanological evidence of the ongoing subduction of Indian Plate along Arakan Trench. *Journal of Volcanology and Geothermal Research*, *360*, 126–138. https://doi.org/10.1016/j.jvolgeores.2018.06.010

Brocher, T. M. (2005). Empirical relations between elastic wavespeeds and density in the Earth's crust. *Bulletin of the Seismological Society of America*, *95*(6), 2081–2092. https://doi.org/10.1785/0120050077

Curray, J. R., Moore, D. G., Lawver, L. A., Emmel, F. J., Raitt, R. W., Henry, M., & Kieckhefer, R. (1979). Tectonics of the Andaman Sea and Burma. In J. S. Watkins, L. Montadert, & P. W. Dickerson (Eds.), *Geological and geophysical investigations of continental margins*, (pp. 189–198). Tulsa, OK: American Association of Petroleum Geologists. https://doi.org/10.1306/m29405c12

Davies, J. H., & Stevenson, D. J. (1992). Physical model of source region of subduction zone volcanics. *Journal of Geophysical Research*, *97*(B2), 2037–2070. https://doi.org/10.1029/91jb02571

Ekström, G., Nettles, M., & Dziewonski, A. M. (2012). The global CMT project 2004–2010: Centroid-moment tensors for 13,017 earthquakes. *Physics of the Earth and Planetary Interiors*, *200–201*, 1–9. https://doi.org/10.1016/j.pepi.2012.04.002

Engdahl, E. R., van der Hilst, R., & Buland, R. (1998). Global teleseismic earthquake relocation with improved travel times and procedures for depth determination. *Bulletin of the Seismological Society of America*, *88*(3), 722–743.

Faccenna, C., Becker, T. W., Lallemand, S., Lagabrielle, Y., Funiciello, F., & Piromallo, C. (2010). Subduction-triggered magmatic pulses: A new class of plumes? *Earth and Planetary Science Letters*, *299*(1), 54–68. https://doi.org/10.1016/j.epsl.2010.08.012

Fukao, Y., & Obayashi, M. (2013). Subducted slabs stagnant above, penetrating through, and trapped below the 660 km discontinuity. *Journal of Geophysical Research: Solid Earth*, *118*(11), 5920–5938. https://doi.org/10.1002/2013jb010466

Global Volcanism Program. (2013). Volcanoes of the world, v. 4.8.2. In E. Venzke (Ed.), Washington, DC: Smithsonian Institution. https://doi.org/10.5479/si.GVP.VOTW4-2013

Hanka, W., Saul, J., Weber, B., Becker, J., Harjadi, P., Fauzi, et al. (2010). Real-time earthquake monitoring for tsunami warning in the Indian Ocean and beyond. *Natural Hazards & Earth System Sciences*, *10*(12), 2611–2622. https://doi.org/10.5194/nhess-10-2611-2010

Hansen, S. E., Evangelidis, C. P., & Papadopoulos, G. A. (2019). Imaging slab detachment within the western Hellenic subduction zone. *Geochemistry, Geophysics, Geosystems*, *20*(2), 895–912. https://doi.org/10.1029/2018gc007810

Hayes, G. P. (2018). *Slab2—A comprehensive subduction zone geometry model*, Golden, CO: U.S. Geological Survey data release. https://doi.org/10.5066/F7PV6JNV

Huang, Z., Wang, L., Xu, M., Zhao, D., Mi, N., & Yu, D. (2019). P and S wave tomography beneath the SE Tibetan Plateau: Evidence for lithospheric delamination. *Journal of Geophysical Research: Solid Earth*, *124*, 10292–10308. https://doi.org/10.1029/2019jb017430

Hurukawa, N., Tun, P. P., & Shibazaki, B. (2012). Detailed geometry of the subducting Indian Plate beneath the Burma Plate and subcrustal seismicity in the Burma Plate derived from joint hypocenter relocation. *Earth Planets and Space*, *64*(4), 333–343. https://doi.org/10.5047/eps.2011.10.011

Ishii, M., Shearer, P. M., Houston, H., & Vidale, J. E. (2005). Extent, duration and speed of the 2004 Sumatra–Andaman earthquake imaged by the Hi-Net array. *Nature*, *435*(7044), 933–936. https://doi.org/10.1038/nature03675

Kennett, B. L. N., Engdahl, E. R., & Buland, R. (1995). Constraints on seismic velocities in the Earth from traveltimes. *Geophysical Journal International*, *122*(1), 108–124. https://doi.org/10.1111/j.1365-246X.1995.tb03540.x

Laske, G., Masters, G., Ma, Z., and Pasyanos, M. (2013), *Update on CRUST1. 0—A 1-degree global model of Earth's crust*, Kastenbauerstr, Munich, Germany: Paper presented at Geophysical Research Abstracts, EGU General Assembly.

Le Dain, A. Y., Tapponnier, P., & Molnar, P. (1984). Active faulting and tectonics of Burma and surrounding regions. *Journal of Geophysical Research*, *89*(B1), 453–472. https://doi.org/10.1029/JB089iB01p00453

Lei, J., & Zhao, D. (2016). Teleseismic P-wave tomography and mantle dynamics beneath Eastern Tibet. *Geochemistry, Geophysics, Geosystems*, *17*(5), 1861–1884. https://doi.org/10.1002/2016gc006262

Liu, X., McNally, K. C., & Shen, Z.-K. (1995). Evidence for a role of the downgoing slab in earthquake slip partitioning at oblique subduction zones. *Journal of Geophysical Research*, *100*(B8), 15351–15372. https://doi.org/10.1029/95jb00870

Liu, S., Suardi, I., Zheng, M., Yang, D., Huang, X., & Tong, P. (2019). Slab morphology beneath northern Sumatra revealed by regional and teleseismic traveltime tomography. *Journal of Geophysical Research: Solid Earth*, *124*(10), 10544–10564. https://doi.org/10.1029/2019jb017625

Li, C., van der Hilst, R. D., Meltzer, A. S., & Engdahl, E. R. (2008). Subduction of the Indian lithosphere beneath the Tibetan Plateau and Burma. *Earth and Planetary Science Letters*, *274*(1), 157–168. https://doi.org/10.1016/j.epsl.2008.07.016

Mallick, R., Lindsey, E. O., Feng, L., Hubbard, J., Banerjee, P., & Hill, E. M. (2019). Active convergence of the India-Burma-Sunda plates revealed by a new continuous GPS network. *Journal of Geophysical Research: Solid Earth*, *124*(3), 3155–3171. https://doi.org/10.1029/2018jb016480

Mishra, S., Prajapati, S., & Teotia, S. S. (2019). Mantle Transition Zones (MTZ) discontinuities beneath the Andaman Subduction Zone. *Journal of Asian Earth Sciences*, *191*, 104102. https://doi.org/10.1016/j.jseaes.2019.104102

Mitra, S., Priestley, K. F., Borah, K., & Gaur, V. K. (2018). Crustal structure and evolution of the Eastern Himalayan Plate boundary system, Northeast India. *Journal of Geophysical Research: Solid Earth*, *123*(1), 621–640. https://doi.org/10.1002/2017jb014714

Müller, R. D., Sdrolias, M., Gaina, C., & Roest, W. R. (2008). Age, spreading rates, and spreading asymmetry of the world's ocean crust. *Geochemistry, Geophysics, Geosystems*, *9*(4), Q04006. https://doi.org/10.1029/2007gc001743

Ni, J. F., Guzman-Speziale, M., Bevis, M., Holt, W. E., Wallace, T. C., & Seager, W. R. (1989). Accretionary tectonics of Burma and the three-dimensional geometry of the Burma subduction zone. *Geology*, *17*(1), 68–71. https://doi.org/10.1130/0091-7613(1989)017<0068:Atobat>2.3.Co;2

Pesicek, J. D., Thurber, C. H., Widiyantoro, S., Zhang, H., DeShon, H. R., & Engdahl, E. R. (2010). Sharpening the tomographic image of the subducting slab below Sumatra, the Andaman Islands and Burma. *Geophysical Journal International*, *182*(1), 433–453. https://doi.org/10.1111/j.1365-246X.2010.04630.x

Pivnik, D. A., Nahm, J., Tucker, R. S., Smith, G. O., Nyein, K., Nyunt, M., & Maung, P. H. (1998). Polyphase deformation in a fore-arc/back-arc basin, Salin subbasin, Myanmar (Burma). *AAPG Bulletin*, *82*(10), 1837–1856.

Prieto, G. A., Beroza, G. C., Barrett, S. A., López, G. A., & Florez, M. (2012). Earthquake nests as natural laboratories for the study of intermediate-depth earthquake mechanics. *Tectonophysics*, *570–571*, 42–56. https://doi.org/10.1016/j.tecto.2012.07.019

Rawlinson, N., Pozgay, S., & Fishwick, S. (2010). Seismic tomography: A window into deep Earth. *Physics of the Earth and Planetary Interiors*, *178*(3), 101–135. https://doi.org/10.1016/j.pepi.2009.10.002

Rawlinson, N., Reading, A. M., & Kennett, B. L. N. (2006). Lithospheric structure of Tasmania from a novel form of teleseismic tomography. *Journal of Geophysical Research*, *111*(B2), B02301. https://doi.org/10.1029/2005JB003803

Rawlinson, N., & Sambridge, M. (2005). The fast marching method: An effective tool for tomographic imaging and tracking multiple phases in complex layered media. *Exploration Geophysics*, *36*(4), 341–350. https://doi.org/10.1071/EG05341

Replumaz, A., Kárason, H., van der Hilst, R. D., Besse, J., & Tapponnier, P. (2004). 4-D evolution of SE Asia's mantle from geological reconstructions and seismic tomography. *Earth and Planetary Science Letters*, *221*(1), 103–115. https://doi.org/10.1016/S0012-821X(04)00070-6

Replumaz, A., Negredo, A. M., Guillot, S., & Villaseñor, A. (2010). Multiple episodes of continental subduction during India/Asia convergence: Insight from seismic tomography and tectonic reconstruction. *Tectonophysics*, *483*(1), 125–134. https://doi.org/10.1016/j.tecto.2009.10.007

Richards, S., Lister, G., & Kennett, B. (2007). A slab in depth: Three-dimensional geometry and evolution of the Indo-Australian plate. *Geochemistry, Geophysics, Geosystems*, *8*(12), Q12003. https://doi.org/10.1029/2007gc001657

Satyabala, S. P. (2003). Oblique plate convergence in the Indo-Burma (Myanmar) subduction region. *Pure and Applied Geophysics*, *160*(9), 1611–1650. https://doi.org/10.1007/s00024-003-2378-0

Sethian, J. A., & Popovici, A. M. (1999). 3-D traveltime computation using the fast marching method. *Geophysics*, *64*(2), 516–523. https://doi.org/10.1190/1.1444558

Singha, P., Dewangan, P., Kamesh Raju, K. A., Aswini, K. K., & Ramakrushana Reddy, T. (2019). Geometry of the subducting Indian Plate and local seismicity in the Andaman region from the Passive OBS Experiment. *Bulletin of the Seismological Society of America*, *109*(2), 797–811. https://doi.org/10.1785/0120180178

Singh, A., Bhushan, K., Singh, C., Steckler, M. S., Akhter, S. H., Seeber, L., et al. (2016). Crustal structure and tectonics of Bangladesh: New constraints from inversion of receiver functions. *Tectonophysics*, *680*, 99–112. https://doi.org/10.1016/j.tecto.2016.04.046

Steckler, M. S., Mondal, D. R., Akhter, S. H., Seeber, L., Feng, L., Gale, J., et al. (2016). Locked and loading megathrust linked to active subduction beneath the Indo-Burman Ranges. *Nature Geoscience*, *9*(8), 615–618. https://doi.org/10.1038/ngeo2760

Tao, K., Grand, S. P., & Niu, F. (2018). Seismic structure of the upper mantle beneath Eastern Asia from full waveform seismic tomography. *Geochemistry, Geophysics, Geosystems*, *19*(8), 2732–2763. https://doi.org/10.1029/2018gc007460

Tong, P., Yang, D., & Huang, X. (2019). Multiple-grid model parametrization for seismic tomography with application to the San Jacinto fault zone. *Geophysical Journal of Intelligence*, *218*(1), 200–223. https://doi.org/10.1093/gji/ggz151

Tong, P., Yang, D., Li, D., & Liu, Q. (2017). Time-evolving seismic tomography: The method and its application to the 1989 Loma Prieta and 2014 South Napa earthquake area, California. *Geophysical Research Letters*, *44*(7), 3165–3175. https://doi.org/10.1002/2017gl072785

Tong, P., Zhao, D., Yang, D., Yang, X., Chen, J., & Liu, Q. (2014). Wave-equation-based travel-time seismic tomography &ndash—Part 1: Method. *Solid Earth*, *5*(2), 1151–1168. https://doi.org/10.5194/se-5-1151-2014

Van der Voo, R., Spakman, W., & Bijwaard, H. (1999). Tethyan subducted slabs under India. *Earth and Planetary Science Letter*, *171*(1), 7–20. https://doi.org/10.1016/S0012-821X(99)00131-4

Wang, X., Wei, S., Wang, Y., Maung, X. P., Hubbard, J., Banerjee, P., et al. (2019). A 3-D shear wave velocity model for Myanmar region. *Journal of Geophysical Research: Solid Earth*, *124*, 504–526. https://doi.org/10.1029/2018JB016622

Wang, Y., Sieh, K., Tun, S. T., Lai, K.-Y., & Myint, T. (2014). Active tectonics and earthquake potential of the Myanmar region. *Journal of Geophysical Research: Solid Earth*, *119*(4), 3767–3822. https://doi.org/10.1002/2013JB010762

Wessel, P., & Smith, W. H. (1998). New, improved version of Generic Mapping Tools released. *Eos, Transactions, American Geological Union*, *79*(47), 579. https://doi.org/10.1029/98EO00426

Xu, M., Huang, H., Huang, Z., Wang, P., Wang, L., Xu, M., et al. (2018). Insight into the subducted Indian slab and origin of the Tengchong volcano in SE Tibet from receiver function analysis. *Earth and Planetary Science Letters*, *482*, 567–579. https://doi.org/10.1016/j.epsl.2017.11.048